X-ray combined analysis of fiber-textured and epitaxial $Ba(Sr,Ti)O_3$ thin films deposited by radio frequency sputtering

D. Rémiens,[1,a)] L. Yang,[1,3] F. Ponchel,[1] J. F. Légier,[1] D. Chateigner,[2] G. Wang,[3] and X. Dong[3]
[1]*IEMN- UVHC - DOAE – MIMM Team – CNRS UMR 8520, Université des Sciences et Technologies de Lille, Bat. P3, BP 60069, 59652 Villeneuve d'Ascq Cedex, France*
[2]*CRISMAT-ENSICAEN, IUT-Caen, Université de Caen Basse-Normandie- 6, Bd. M. Juin 14050 Caen, France*
[3]*Key Laboratory of Inorganic Functional Materials and Devices Shanghai Institute of Ceramics, Chinese Academy of Sciences, 1295 Dingxi Road, Shanghai 200050, China*

(Received 22 October 2010; accepted 16 April 2011; published online 9 June 2011)

A complete study is given in this paper on the structural properties of $Ba(Sr,Ti)O_3$ (BST) thin films which present various preferred orientations: (111) and (001) fiber and epitaxial textures. The films are deposited *in situ* at 800 °C by sputtering on $Si/SiO_2/TiO_x/Pt$ substrates and the orientation is controlled by monitoring the concentration of O_2 in the reactive plasma or by prior deposition of a very thin TiO_x buffer layer between BST films and substrates. The epitaxial films are obtained on (001)-alpha-Al_2O_3 substrates covered with TiO_x buffer layers. In order to analyze finely the preferred orientations, the texture, the microstructural features, and the anisotropy-related quantities such as residual stresses in the films, the conventional Bragg−Brentano θ - 2θ x-ray diffraction diagrams is shown not to be sufficient. So, we systematically used x-ray combined analysis, a recently developed methodology which gives access to precise determination of the structure (cell parameters and space group) of the films, their orientation distributions (texture strengths and types) and mean crystallite sizes, their residual stresses. This fine structural analysis shows important modifications between the film qualities which induce differences in BST films electrical behavior, permittivity, loss tangent, and tunability. © *2011 American Institute of Physics*. [doi:10.1063/1.3592282]

I. INTRODUCTION

$Ba(Sr,Ti)O_3$ (BST) compounds have become the leading materials for microwave device applications such as decoupling capacitors and microwave tunable devices, including tunable mixers, delay lines, filters, and phase shifters for steerable antennas.[1–3] The main reasons for these are due to their high dielectric response and tunability, even at very high frequencies, near the ferroelectric phase transition temperature. Several compositions of BST thin films have been studied in great details using a variety of different fabrication methods (sol gel, pulsed laser deposition, sputtering).[4–7] It is well known that the performances of the films as well in terms of losses as in tunability are in relation with the structural properties of the films.[8–10] For example the dielectric tunability is larger for (111) oriented films compared to (001) and the best electrical properties are obtained on (001) epitaxial BST films.[11,12] In this context, it is important to compare the structural and the microstructural properties of BST films exhibiting (001) and (111)-preferred orientations, as fiber- or epitaxial textures. The residual stresses in the films, which are certainly different between films differently oriented, have also a non-negligible effect on the films tunability. To our knowledge no study has been dedicated to a detailed determination of structural, textural, microstructural characteristics of differently oriented BST films. In this work, depending on the reactive sputtering conditions (Ar/O_2 ratio) and the presence of a TiO_x buffer layer, we obtain BST films with various preferred-orientations, i.e., (111) fiber (type 1) and (001) fiber (type 2) textures, respectively. On (001)-alpha-Al_2O_3 substrates we demonstrate the possibility to stabilize epitaxial BST textures. Rapidly we show that the conventional Bragg−Brentano θ- 2θ x-ray diffraction diagrams do not allow the quantitative determination of preferred orientations, microstructural features, and anisotropy-related quantities such as residual stresses. This clearly indicates limitation in using the Lotgering factors for a detailed analysis, otherwise of practical use. In this paper, we systematically used x-ray combined analysis, a recently developed methodology which gives access to precise determination of the structural quality of the films (encompassing texture, structure, crystallite sizes, residual stresses. analyses),[13,14] in order to correlate these parameters with the films properties.

II. EXPERIMENTAL PROCEDURES

The BST films composition is fixed to 60/40 for the Ba/Sr ratio, and the films are deposited by radio frequency (rf) sputtering (*in situ* process at 800 °C) on $Si/SiO_2/TiO_x/Pt$ and sapphire substrates covered with or without a TiO_x (with $x \rightarrow 2$) buffer layer. A first characterization of the BST target carried out under the P4 mm space group indicated cell parameters of $a = 3.9386(7)$ Å and $c = 3.955(1)$ Å coherent with the expected values for the targeted composition. We

a)Author to whom correspondence should be addressed. Electronic mail: denis.remiens@univ-valenciennes.fr.

also detected residual carbonates in the target. The sputtering conditions of the BST films deposited on $Si/SiO_2/TiO_x/Pt$ and sapphire substrates are given in Table I. Only the growth rate was varied (using different OMR values), and in particular the growth temperature was kept identical, independently of the presence or not of the buffer layer. The sputtering conditions of the TiO_x buffer layer are presented in Table II, and the thickness of the films is controlled by the sputtering time. After deposition, we operate systematically a post annealing treatment (700 °C) under oxygen in order to saturate the oxygen content of the buffer layer ($TiO_x \rightarrow TiO_2$) as much as possible, however without stoichiometry measurement. We then prefer to use TiO_x rather than TiO_2 to indicate the composition of the buffer layer. The structures of the BST films are analyzed by two approaches: the classical "conventional" θ-2θ diffractometry in the Bragg−Brentano geometry (using only Ni-filtered Cu-K radiation – Si calibration) rapidly evidenced limitations to carry out quantitative information about the fiber textures between the different films. We then used a more suitable alternative which takes into account all the targeted parameters (texture, crystallite sizes, stresses, etc.), which will allow the differentiation between textural types, existence and level of residual stresses, variations in films crystallinity. Such a new approach has been recently developed, making use of a x-ray four-circles diffractometer setup equipped with a curved position sensitive detector (CPS120 from INEL SA), and using the monochromatized Cu-K radiation, as described in details elsewhere,[13] and within the combined analysis formalism[14] implemented in the MAUD software.[15] The method is much more complete than simple omega- or phi-scan measurements, as often used to described textures,[16,17] and allows quantitativity of all derived parameters together with their corresponding errors propagated through refinement procedures. Also, it not only provides with a texture correction term for the measured diagrams,[18] but interprets the texture in terms of an orientation distribution.[19,20]

Briefly, this methodology allows the quantitative texture determination of the samples, using a cyclic Rietveld refinement of a series of x-ray diagrams measured at different sample orientations $y_{io}(\omega, \chi, \varphi)$. Each diagram is modeled using the usual (ω,χ,φ)-dependent Rietveld formulation, the y_{ic} calculated intensity profile of each measured diagram $y_{io}(\omega,\chi,\varphi)$ diagram measured at point i ($i = 2\theta$ or any other variable), under (χ,φ) and an incident angle ω:

TABLE I. Typical sputtering conditions of BST thin films on $Si/SiO_2/TiO_x/Pt$.

Target-substrate distance (mm)	80
Substrate temperature (°C)	800
Target	$Ba_{0.6}Sr_{0.4}TiO_3$ ceramic containing excess BaO and SrO
Power density (W/cm^2)	1.58
Deposition pressure (mTorr)	15
OMR ($Ar + O_2$) (%)	from 0% to 50%: 0-10-20-30-40-50
Growth rate (nm/min)	2.60-2.00-1.80-1.50-1.35-1.10
Base pressure (Torr)	$< 2 \times 10^{-6}$

TABLE II. sputtering conditions of TiO_x buffer layer.

Deposition pressure (mTorr)	15
Power density (W/cm^2)	1.60
Substrate temperature (°C)	Room temperature (post annealed at 700°C)
$O_2/Ar + O_2$ (%)	20
Thickness (nm)	1-2-5-7-12-20

$$y_{ic}(\omega,\chi,\varphi) = y_{ib}(\omega,\chi,\varphi) + \sum_{\Phi=1}^{N_\Phi} S_\Phi \times \sum_{k=K_1}^{K} j_{\Phi k} Lp_{\Phi k} P_{\Phi k}(\omega,\chi,\varphi)|F_{\Phi k}|^2 \times \Omega_{i\Phi k} A_{i\Phi}(\omega,\chi,\varphi) \quad (1)$$

This profile is compared to the observed y_{io} profile, and the calculated diagrams are adjusted to observations using for instance a nonlinear least-squares minimization technique. In this equation the various variables are:

- $j_{\Phi k}$ the multiplicity factor of the peak for phase Φ
- $Lp_{\Phi k}$ the Lorentz-polarization factor
- $P_{\Phi k}$ the correction factor describing preferred orientations of phase Φ
- $|F_{\Phi k}|$ the modulus of the structure factor (including thermal vibrations) of phase Φ
- $\Omega_{i\Phi k}$ the profile function of the peaks of phase Φ, which represents instrumental and potential sample broadenings due to crystallite finite sizes and micro strains
- $A_{i\Phi}$ the absorption factor which takes into account the experimental and sample geometries, like layer thicknesses for instance

Due to the expected texture strength in such materials, we measured two sets of 2θ diagrams. 936 diagrams were measured using a regular $5° \times 5°$ grid in tilt and azimuth angles (χ and φ, respectively) with $0 \le \chi \le 60°$ and $0 \le \varphi \le 355°$, and 863 diagrams in the $2.5 \le \chi \le 57.5°$, and $2.5 \le \varphi \le 357.5°$ ranges with the same steps. For both sets an incident angle of the x-ray beam on the sample of $\omega = 19.5°$ was chosen, centered on the 111 reflection of BST. The instrument contributions (χ and ω broadenings, peak shapes, zero-shifts, line shapes.) were calibrated using the 660b LaB_6 powder standard from NIST. A counting time of 2 min for each sample orientation was used, and our optical setup provides with a 0.1° peak widths in 2θ around $2\theta = 40°$.

Preferred orientation (texture) factors entering each diagram are obtained from integrated intensities. These latter are extracted using the texture-adapted Le Bail approach,[21] a way of obtaining integrated intensities of individual reflections k from powder diagrams exhibiting a lot of overlaps:

$$I_{o,k} = \sum_i \frac{(y_{io} - y_{ib}) W_{ik} I_{c,k}}{(y_{ic} - y_{ib})} \quad \text{with } y_{ic} = \sum_k W_{ik} I_{c,k} \quad (2)$$

In Eq. (2), W_{ik} takes into account all other factors like scale, multiplicity of the line, Lorentz-polarization factors, peak-shape function…, and $I_{c,k}$ is calculated from the initial orientation distribution function [ODF or $f(g)$]. The initiated $I_{c,k}$ values are forced to the same weight, i.e. 1 (randomly

oriented sample). In the following cycles, the $I_{o,k}$ values previously obtained are substituted to the $I_{c,k}$ of the decomposition formula. During the iterations the least-squares procedure then forces the respective intensities to become coherent with the observed overlap, and progressively converge to the observed intensities. The extracted intensities are then finally obtained directly from the observation best fit, and serve texture factor for next ODF [$f(g)$] refinements.

Pole figures obtained here [$P_{\mathbf{h}}(\mathbf{y})$: with $\mathbf{h}=[hk\ell]^*$ the normal to the diffracting planes and $\mathbf{y}$ the orientation of this normal in the sample frame], are normalized into multiples of a random distribution (m.r.d.), a unit that does not depend on other factors than orientation. In such units, a sample without preferred orientations exhibits uniform pole figures with 1 m.r.d. levels, while a textured sample shows pole figures with maxima and minima of orientation densities ranging from 0 m.r.d. (absence of crystals oriented in this direction) to infinity (for a single crystal on few directions). The overall texture strength is evaluated through the texture index[22,23] $F^2 = \frac{1}{8\pi^2}\sum [f(g_i)]^2 \Delta g_i$, g_i being the i orientation cells, which is expressed in m.r.d.^{2} units and varies from 1 (random powder) to infinity (perfect texture or single crystal) and used to compare the texture strength of different samples exhibiting similar Orientation Distributions. Such normalized pole figures are calculated from $f(g)$, this latter being refined for the BST and Pt layers using the E-WIMV formalism[24] after extraction of the peak intensities during the Rietveld cycles. The E-WIMV approach can be used with irregular coverage of the OD space, and provides with an iterative scheme of the OD refinement which is very close to the maximization of entropy.[25] This method is then often called Entropy-modified WIMV.[13] The OD cell values are computed through an entropy iteration algorithm that includes the reflection weights:

$$f^{n+1}(g) = f^n(g) \prod_{h=1}^{I} \prod_{m=1}^{M_h} \left(\frac{P_h(\mathbf{y})}{P_h^n(\mathbf{y})} \right)^{r_n \frac{w_h}{IM_h}} \tag{3}$$

where the product extends over the I experimentally measured pole figures and for all the poles multiplicity $M_{\mathbf{h}}$, $f^n(g)$ and $P_{\mathbf{h}}^{n}(\mathbf{y})$ represent the refined values of $f(g)$ and $P_{\mathbf{h}}(\mathbf{y})$ at the nth step respectively, r_n is a relaxation parameter such that $0 < r_n < 1$, and the reflection weight $w_{\mathbf{h}}$ is introduced to take into account the different accuracy of the more intense and less overlapped reflections with respect to the smaller ones, and is calculated analogously to the weight factors of the Rietveld analysis. This approach proved its efficiency.[13,24,26,27] As we can see from Eq. (3), this method consists on a convergent geometrical mean from the ratio of measured pole figures to the one measured at the n^{st} step of the refinement. The initial $n=0$ estimate of $f(g)$ is operated through the same scheme as for the usual WIMV procedure:[22]

$$f^0(g) = N_0 \left(\prod_{\mathbf{h}=1}^{I} \prod_{m=1}^{M_h} P_{\mathbf{h}}^{\exp}(\mathbf{y}) \right)^{\frac{1}{IM_{\mathbf{h}}}} \tag{4}$$

in which $P_h^{\exp}(y)$ stands for the measured pole figures. The number N_0 is a normalizing factor, and the $P_h^n(\mathbf{y})$ values are calculated at each cycle using the fundamental equation of texture analysis:[22]

$$P_{\mathbf{h}}(\mathbf{y}) = \frac{1}{2\pi} \int_{\mathbf{h}//\mathbf{y}} f(g) d\tilde{\varphi} \tag{5}$$

This equation represents the fact that each pole figure (a 2D object) is a projection along a certain path $\tilde{\varphi}$ of the ODF (a 3D object). Each cell of a given pole figure is an average over several cells of the ODF, and each cell of the ODF is measured by one or more cells from the pole figures. The larger the number of pole figure cells that measure a specific ODF cell and the more statistically reliable is the measurement of this ODF. In practice, one has to measure the largest number as possible of reliable (enough intense) pole figures to define the ODF with the best available resolution. This latter condition is fulfilled using a whole pattern analysis as practiced in the Combined Analysis approach.

The OD and profile refinement reliabilities are estimated using conventional reliability factors.[28]

During these refinements we used either the unit-cell definition of BST corresponding to the cubic Pm3 m or to the tetragonal P4 mm space groups, depending on which group resulted in lower reliability factors after refinements, and the nominal Ba/Sr ratio of 0.65/0.35. We started the refinements from the initial phase structural models of the crystallography open database (n° 2100858, n° 2100862, and n° 1011103 for BST-P4 mm, BST-Pm3 m and Pt-Fm3 m, respectively).[29] For the BST films deposited on (001)-alpha-Al_2O_3 (001) substrate, the sample reference frame is given by the corundum substrate, for which a Gaussian standard function[22] with 0.5° of FWHM was used to simulate the orientation. For the BST films deposited on platinized Si substrates fiber textures were observed for both the BST and Pt layers, and no simulation of the Si texture was used. In the pole figures shown in this work, the normal to the film surface corresponds to the center of the pole figures. The $\sigma^{M}{}_{11}$ and $\sigma^{M}{}_{22}$ macroscopic residual stresses in the film plane were refined using the macroscopic measured deformations $\varepsilon^{M}{}_{kl}$ and the film elastic stiffness $C^{M}{}_{ijkl}$. These latter were simulated from the OD and the single crystal elastic stiffness of BST and Pt, using the geometric mean approach,[30] at each refinement step. The geometric average of stiffness constants over orientations, i.e. the macroscopic stiffness of the polycrystal is calculated from:

$$\begin{aligned} C_{ijkl}^{M} &= \exp\left(\langle \ln C \rangle_{i'j'k'\ell'} \right) \\ &= \exp\left(\langle \Theta \rangle_{ijk\ell,i'j'k'\ell'} (lnC)_{i'j'k'\ell'} \right) \end{aligned}$$

with

$$\langle \Theta \rangle_{ijk\ell,i'j'k'\ell'} = \int_{g} \Theta_i^{i'}(g) \Theta_j^{j'}(g) \Theta_k^{k'}(g) \Theta_\ell^{\ell'}(g) f(g) dg$$

and $(\ln C)_{i'j'k'l'}$ is given by:

$$\begin{aligned} (\ln C)_{ijk\ell} &= \sum_{\lambda=1}^{6} \ln(\mathbf{C}^{(\lambda)}) \mathbf{b}_{ij}^{(\lambda)} \mathbf{b}_{k\ell}^{(\lambda)} \\ &= \ln \left[\prod_{\lambda=1}^{6} (\mathbf{C}^{(\lambda)})^{\mathbf{b}_{ij}^{(\lambda)} \mathbf{b}_{k\ell}^{(\lambda)}} \right] \end{aligned}$$

where the (λ) exponent denotes eigenvalues of the corresponding quantities, and the $b_{ij}^{(\lambda)}$ are the eigentensors resulting from diagonalization of the arithmetic average $\langle \ln C \rangle_{i'j'k'l'}$ for the oriented polycrystal.[31] The four successive tensor transformations relate to the 4th order stiffness tensor character. The factorial entering the calculation explains the term "geometric mean," in the sense that the oriented polycrystal macroscopic stiffness is obtained by the mean averaging of the single crystal stiffness eigenvalues. Similar expressions could be obtained for the macroscopic compliance tensor S_{ijkl}^{M} which admits as eigenvalues $S^{(\lambda)} = 1/C^{(\lambda)}$ the reciprocal of the stiffness eigenvalues. This warrants that the same macroscopic elastic properties are calculated when using stiffness or compliances in the geometric mean approach. In other words, the average of the inverse macroscopic property is consistent with the inverse of the average macroscopic property. This may be the reason why this modeling gives rather good estimates of the elastic properties,[30] comparable to ones obtained by more sophisticated models which require larger calculation times, somehow less suitable for implementation in routinely achieved combined algorithm.[32–35]

We have used the single crystal elastic stiffness constants of cubic BST at $c_{11} = 195.31$ GPa, $c_{44} = 170.65$ GPa, and $c_{12} = 60.6$ GPa,[36] of Pt at $c_{11} = 289$ GPa, $c_{44} = 65$ GPa, and $c_{12} = 239$ GPa.[37] Isotropic and anisotropic crystallite sizes and microstrains were refined in the Rietveld cycles, after direct deconvolution and Fourier analysis of the peak profiles.[14] The microstructure of the films is observed by scanning electron microscopy (SEM).

III. RESULTS AND DISCUSSION

The introduction of O_2 in the plasma (reactive sputtering $Ar + O_2$) has a strong influence on the film orientation as shown in the x-ray diffraction spectra [Fig. 1(a)], using a conventional θ-2θ diffractometer in the Bragg–Brentano geometry (using only Ni-filtered Cu- monochromatized Cu-K radiation – Si calibration). Without O_2 the films exhibit a preferred (001) orientation while a (111) orientation component develops when increasing the O_2 content in the plasma. The typical degree of orientation, as seen from the Lotgering factor $\alpha(111)$, reaches 100% for an oxygen mixing ratio (OMR) of 30% (Fig. 2); the OMR correspond to the ratio $P(O_2)/P(O_2) + P(Ar)$. The insert of Fig. 2 shows the variation of the growth rate as a function of the OMR. In this study film thicknesses are identical (400 nm) whatever the sputtering conditions (OMR), thanks to a sputtering time adjustment to maintain the same film thickness. The introduction of oxygen in the plasma has also a strong influence on the lattice parameters of BST as presented in Table III. However, if the α_{111} factor saturates for O_2 amounts larger than 30%, the (111)-BST peaks decrease compared to their largest value. This clearly indicates a limitation in using the Lotgering factors for a detailed analysis, otherwise of practical use. The change of preferred orientation of BST films on $Pt/TiO_x/SiO_2/Si$ from (001) to (111) with various OMR can be explained in terms of competing surfaces and interface energies during nucleation. The high growing temperature (800 °C) and the relatively low film growth rates (~2.6 nm/min), corresponding to OMR = 0% probably favor (001) nuclei with low surface energy under thermodynamic conditions.[37] However, the interface role seems to dominate since oxygen presence during sputtering caused insufficient impingement of ad-atoms on the substrate (low growth rate, <2 nm/min), hence, the atoms are forced to take next energetically favorable configuration, i.e., BST(111), imposed by the top layer of the $Pt(111)/TiO_x/SiO_2/Si$ substrate. Another possible explanation could be the increase of the BST lattice parameters with OMR (Table III) which favors the change of orientation, as pointed out by some authors.[38,39]

The OMR has a strong influence on the electric properties of the films. Figure 3 and Table IV show the variation of the relative permittivity, the loss factor and the tunability as a function of the OMR. The permittivity attains a maximum value for 30% O_2 and the tunability reaches a maximum value of 26% for this O_2 content in the plasma.

The microstructures of the films [Fig. 4(a)], as seen with SEM, show large surface roughness for the (001) BST films, while the grain sizes of the (111) BST films appear smaller than the (001) ones [Fig. 4(c)].

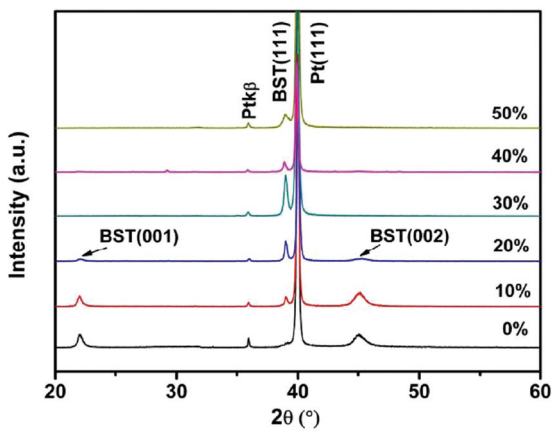

FIG. 1. (Color online) XRD patterns of BST thin films deposited at 800 °C on Si/SiO2/TiO_x/Pt substrate with various O_2 content in the plasma.

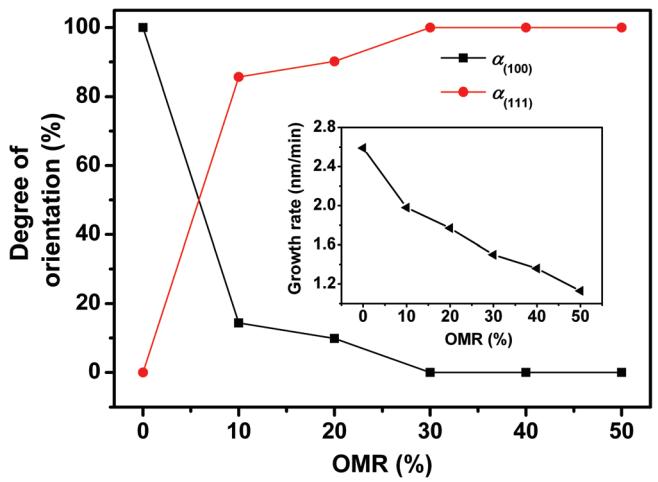

FIG. 2. (Color online) Degree of orientation and growth rate of BST films with various OMR (oxygen mixing ratio). The insert of Fig. 2 shows the evolution of the growth rate as a function of the OMR.

TABLE III. Evolution of the BST lattice parameters as a function of OMR.

OMR (%)	a (Å)	c (Å)	a_0 (Å)	$\alpha_{(001)}$ (%)	$\alpha_{(111)}$ (%)
0	—	4.017	—	100	0
10	3.980	4.024	3.995	14.36	85.64
20	3.978	4.028	3.995	9.85	90.15
30	—	—	3.995	0	100
40	—	—	4.005	0	100
50	—	—	4.007	0	100

BST ($BaSrTiO_3$), OMR = $O_2/Ar + O_2$ mixing ratio.

TABLE IV. Evolution of tunability and FOM as a function of OMR.

OMR (%)	Permittivity	tan δ at zero field	Tunability (%) at 400 kV/cm	FOM
0	346.06	0.0149	52.12	34.98
10	432.34	0.0215	58.94	27.41
20	503.96	0.0213	60.56	28.43
30	631.42	0.0261	67.82	25.98
40	561.69	0.0209	62.49	29.89
50	469.21	0.0212	59.02	27.83

Another classical approach to control the film orientation is the use of a TiO_x buffer layer on the Pt(111)/TiO_x/SiO_2/Si substrate. The sputtering conditions of the TiO_x buffer layer are given in Table II. The sputtering conditions of BST films are similar to those previously described except the absence of oxygen in the plasma, in order to show that the control of the orientation is induced by the TiO_x layer and not by the OMR. The BST film thicknesses are the same whatever the TiO_x buffer layer (400 nm). An important result is the change in BST film orientation upon the thickness of the TiO_x buffer layer (Fig. 5); the x-rays diffraction peaks relative to TiO_x cannot be observed due to the lack of resolution of our θ-2θ diffractometer or due to the poorly crystallization of the very thin film. Without TiO_x, the films exhibit a pronounced (001) preferred orientation while, for a thickness as small as 1.2 nm of TiO_x the BST (111) preferred orientation is revealed. The introduction of TiO_x gives rise to similar diffraction diagrams as the ones observed for films with introduction of oxygen in the Ar plasma, with corresponding evolutions of the α(001) and α(111) factors as a function of the TiO_x buffer layer thickness. Considering only the peak intensities of the θ-2θ diagrams, the TiO_x thickness to obtain the strongest (111)-BST peak is 5 nm. This peak decreases for larger buffer thicknesses (while Lotgering factors saturate), without apparition of any other peak. This could be attributed to a peak broadening due to smaller crystallite sizes, to the development of other texture components not visible in the available 2θ range, to a tilt of the (111) component, and to a decrease in crystallinity. Some authors have been also published similar studies,[40–42] i.e., introduction of a TiO_x buffer layer before the growth of BST films, but the results are different than those present in this paper. The presence of a TiO_x buffer layer reinforced the (110) orientation of BST films and does not changed the film orientation as in our study; it is very difficult to compare the buffer layer effects since the thicknesses of the buffer layer and the films BST, the growth technique deposition, the substrate etc are different. The change in orientation and crystallinity of the BST films is related to the growth mode of BST perovskite film by the insertion of a buffer layer, in association with the expected underlying substrate and the resulting interface properties. The additional TiO_x on the Pt (111) surface serves as an initial template layer which in turn, results in minimizing the activation energy for surface nucleation during the perovskite crystallization. Meanwhile, the TiO_x layer plays an active role in increasing the number of active sites for BST nucleation and facilitates the perovskite crystallization phase along the orientation of TiO_x/Pt(111)/TiO_x/SiO_2/Si substrate more easily to cause (111)-oriented BST films.[43,44] A comparison of the films surface microstructures with or without the presence of the buffer layer on Pt(111)/TiO_x/SiO_2/Si (Fig. 6) shows larger grain sizes and better uniformity with the presence of the buffer layer compared to BST (001). The BST lattice parameters are also affected by the presence of the TiO_x buffer layer (Table V) and this modification could also be responsible of the preferred orientation modification. As reported by Li *et al.* in TiO_2 seeded $Bi_{3.15}Nd_{0.85}Ti_30_{12}$ films,[45] the main reason for this can be ascribed to the decrease in nucleation energy during film

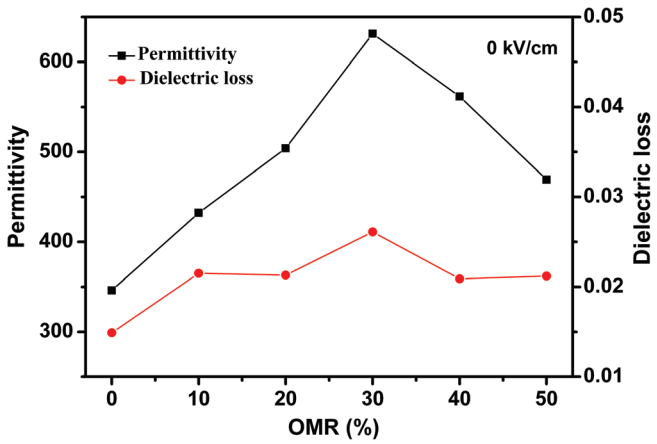

FIG. 3. (Color online) Evolution of the relative dielectric constant, the loss factor and the tunability as a function of the OMR.

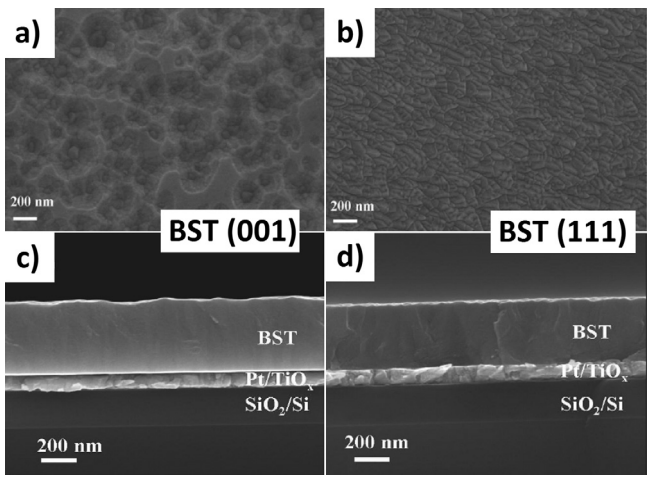

FIG. 4. Surface and cross section SEM photographs of (001)-oriented BST (OMR = 0%) and (111)-oriented BST film (OMR = 30%).

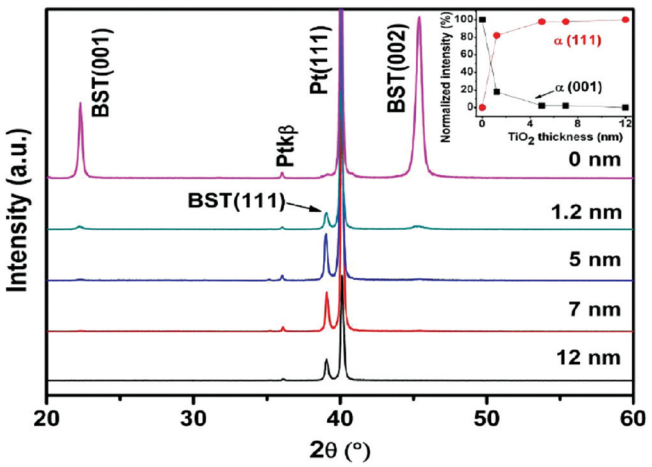

FIG. 5. (Color online) XRD of BST thin films on $Si/SiO_2/TiO_x$/Pt (111) substrates buffered with different thickness of TiO_x seeding layer. The insert of Fig. 4 shows the evolution of the degree of orientation (001) and (111) as a function of the OMR.

growth process. Figure 7 illustrates the electrical properties evolution as a function of the TiO_x buffer layer thickness; the permittivity and the tunability reach maximum values of 500 and 61%, respectively for a 5 nm thick TiO_x buffer layer.

To obtain epitaxial BST films we have used the same processing conditions (without the introduction of oxygen in the plasma) as for the previous films, but the deposition was made directly on (001)-alpha-Al_2O_3 substrate buffered with a TiO_x seeding layer [Al_2O_3 (0001)/TiO_x]. We have not studied the possibility to obtain epitaxial films with the introduction of O_2 in the plasma (OMR); this study could be made in the future. We compare in Fig. 8 the typical x-ray diffraction patterns of BST films deposited on Al_2O_3 - alpha (0001) or Al_2O_3 - alpha (0001)/TiO_x, for a TiO_x and BST films thickness of 5 and 450 nm, respectively. With the TiO_x buffer, a pronounced (111) preferred orientation is evidenced, with

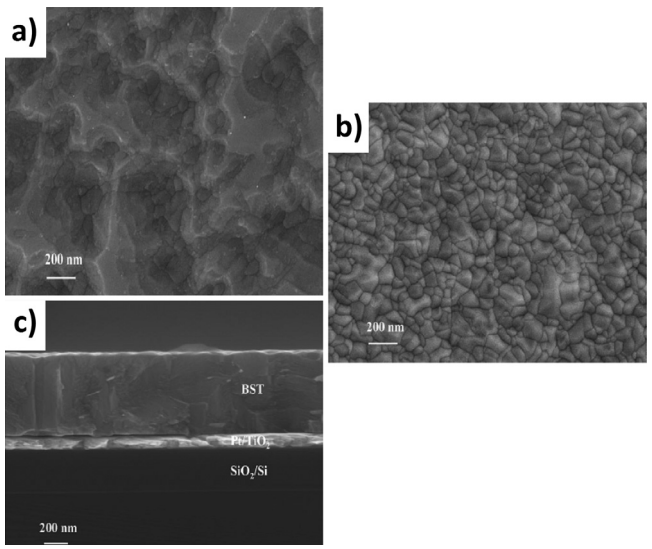

FIG. 6. Surface and cross-section of BST films deposited on $Si/SiO_2/TiO_x$/Pt with or without TiO_2 buffer layer. The thickness of the buffer layer is fixed to 5 nm in this example.

TABLE V. Evolution of the BST lattice parameters as a function of the TiO_x buffer layer thickness.

TiO_2 (nm)	a (Å)	c (Å)	$a0$ (Å)	α(001) (%)	α(001) (%)
0	—	3.982	—	100	0
1.2	3.986	3.999	3.991	17.88	82.12
5	3.985	4.003	3.991	2.22	97.78
7	3.984	3.986	3.985	2.23	97.77
12	—	—	3.987	0	100

$\alpha(111) = 100\%$, while without TiO_x and in pure Argon all the other BST peaks are exhibited, as a sign of more randomly oriented crystallites (polycrystalline film). For instance, comparing Fig. 5 (with a 5 nm buffer inserted) and Fig. 8, one cannot see textural differences [and $\alpha(111) = 100\%$ in both cases] for BST, while an important difference exists as will be evidenced later. Consequently, using x rays, a measurement more complete than a single θ -2θ diagram has to be carried out, and the corresponding analysis which takes into account all the targeted parameters (texture, crystallite sizes, stresses, etc) has to be used, which will allow the differentiation between textural types, existence and level of residual stresses, variations in films crystallinity. Strong variations of diffracted intensities are observed with the (χ,φ) orientation of the BST film deposited on (001)-alpha-Al_2O_3 substrate covered with a very thin (5 nm) TiO_x buffer layer (Fig. 9, bottom). This indicates the presence of a strong texture in the BST film. In particular, each diffracted line exhibits a periodic behavior as a sign of heteroepitaxial relationships with the substrate. Combined analysis refinement (Fig. 9, top) correctly reproduces the experimental diagrams, within reliability factors $R_w = 42.6\%$ and $R_{exp} = 32.5\%$. Such factors could appear large. However one has to bear in mind that reliability factors depend on the number of experimental points, which in our case is very large (around 2.3×10^6 s). From these two factors one can evaluate a χ^2 value of 1.7, corresponding to good refinement values. The pole figures for the main crystallographic directions of BST (Fig. 10) are showing a strong epitaxial-like

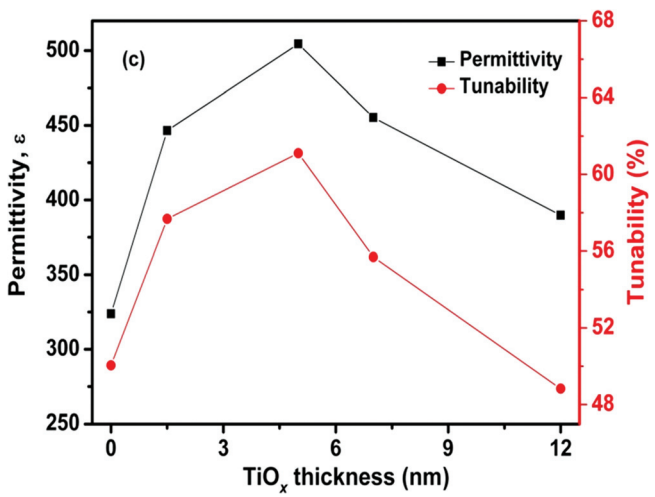

FIG. 7. (Color online) Evolution of the relative dielectric constant and tunability as a function of the TiO_x buffer layer thickness.

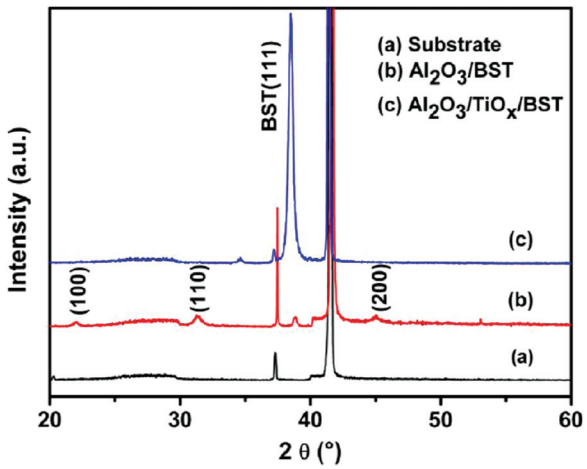

FIG. 8. (Color online) XRD of BST thin films on (001)-alpha-Al_2O_3 substrates buffered with or without a TiO_x buffer layer (5 nm thick).

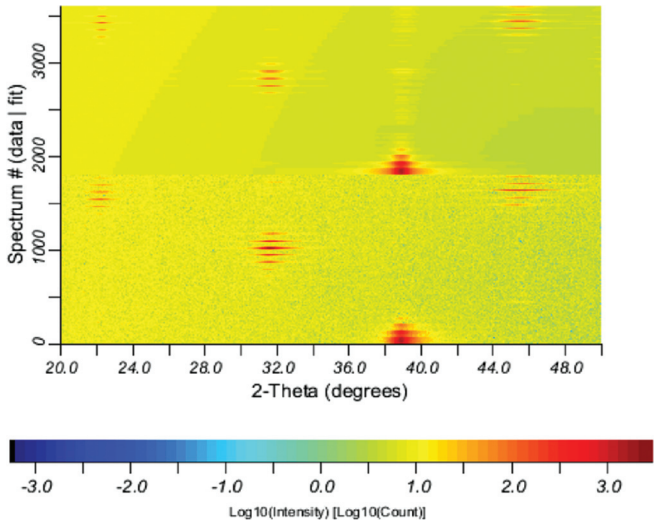

FIG. 9. (Color online) Evolution of the 2θ diagrams with the orientation (χ,φ) of the BST films deposited on (001)-alpha-Al2O3 substrate with a very thin TiOx buffer layer (5 nm) (vertical scale). The bottom set is the 1799 measured diagrams, while the top set are the fits.

character; the presence of the buffer layer, in this thickness range, has no effect on the epitaxial quality of the film. For thicker TiO_x buffer layer (>10 nm) we have not yet made the measurements. A maximum of the OD of 306 m.r.d. is exhibited, corresponding to the nearly 55 m.r.d. maximum value of the {100} pole figure. The OD has also been refined with the satisfactory reliability factors $R_w = 2.7\%$ and $RB = 3.3\%$. The exhibited texture corresponds to [111] directions aligned with the normal to the sample plane ([001] - alpha Al_2O_3 direction), with [110]-BST directions aligned parallel to [100]- alpha Al_2O_3 in the sample plane. This heteroepitaxial relationship corresponds to only 3% of mismatch between d220-BST and d300-Al2O3, giving rise to a sixfold orientation component. The orientation density along the epitaxial direction reaches 32 m.r.d., a value which compares favorably with the ones achieved in other hetero epitaxial oxide films.[46,47] The refinement converges to a unit-cell parameter of 4.00817(3) Å, a value larger by around 0.05 Å compared to the bulk value for the same composition. This unstrained value would point to a slightly lower substitution of Ba for Sr in the structure. An isotropic mean crystallite size of 463.7(9) Å, only half of the total nominal film thickness, indicates the good crystallization of the BST film in coherence with the achievement of heteroepitaxy, and a relatively low level of mean isotropic micro strains at 10^{-4} rms.

We obtained macroscopic sample residual stresses $\sigma^M{}_{11} = -2.33(2)$ GPa and $\sigma^M{}_{22} = -2.40(2)$ GPa in the BST layer. Such level of residual stresses in hetero epitaxially deposited films is not unusual[14] and their compressive character can be understood from the difference between the d220-BST and d300-Al2O3 spacing's.

For the BST films, (named film type 1 and film 2 for respectively (111) and (001)-preferred orientation), deposited, with the reactive deposition process, on $Si/SiO_2/TiO_x/Pt$ substrate the measured diagrams also exhibit strong intensity variations, though an absence of periodic behavior, as a strong sign of fiber texture stabilization for both BST and Pt (Fig. 11 bottom). The bottom set corresponds to the 1799 measured diagrams, while the top set are the fits. The obtained simulation (Fig. 11 top) also satisfactorily compare with the observed diagrams, with $R_w = 27.8\%$, $R_{\exp} = 22.1\%$, and $\chi^2 = 1.57$ for the Rietveld fits and for the ODs, $R_w = 0.8\%$, $R_B = 1.5\%$ for the Pt layer and $R_w = 72\%$, $R_B = 23\%$ for BST. As predicted from the 2θ diagrams, both BST and Pt exhibit strong fiber textures (Fig. 12). In film of type 1, the only fiber component corresponds to [111] directions of both phases aligned with the sample normal. The orientation densities for BST and Pt are correspondingly maximum for the sample's normal, with 25.4 and 25.7 m.r.d., respectively, on the {111} pole figures.

However the overall texture strength in the BST layer is slightly larger, as revealed by an OD maximum of 160 m.r.d. and a texture index F^2 of 12 m.r.d^2, vs 103 and 17 m.r.d^2 respectively in the Pt layer. This indicates the presence of several very minor (the OD minimum is 0 m.r.d.) texture components in Pt. The refined cell parameters of BST

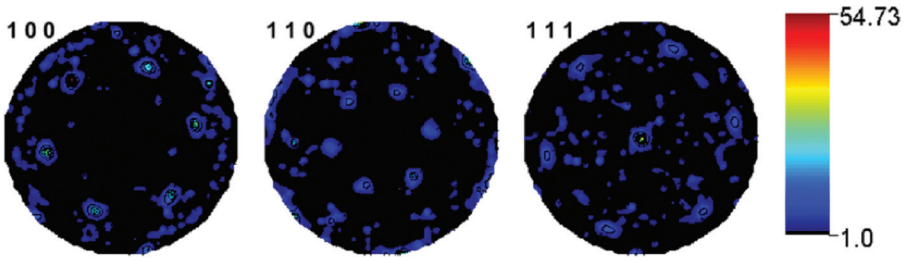

FIG. 10. (Color online) {100}, {110}, and {111} pole figure of BST. Linear density scale, equal-area density projections.

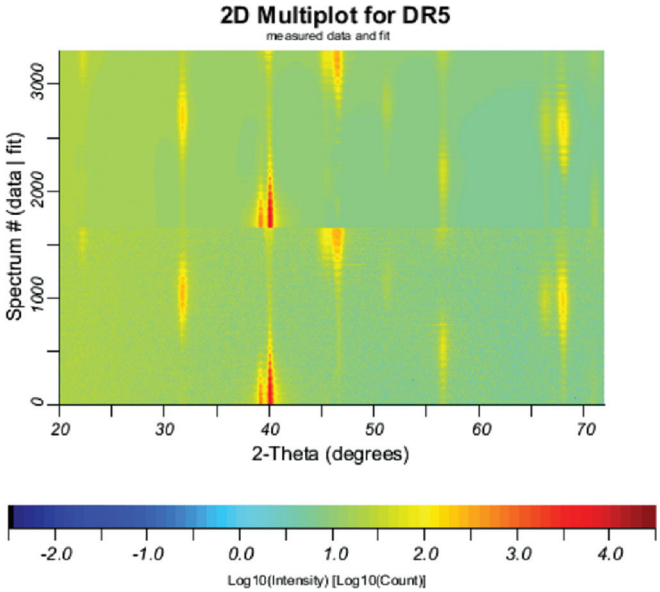

FIG. 11. (Color online) Evolution of the 2θ diagrams with the orientation (χ,φ) of the BST/Pt/Si samples, i.e., type 1 — (111) preferred orientation (vertical scale). The bottom set is the 1799 measured diagrams, while the top set are the fits.

and Pt are $a = 3.96447(5)$ Å and $c = 3.99892(7)$ Å, and $a = 3.90023(1)$ Å respectively, coherent with the bulk values for these phases. A better refinement could be obtained for both the OD and the Rietveld stages when using the BST (P4 mm space group), compared to the cubic phase in this type of film. Since an anisotropic line broadening was observed for the BST phase, the mean crystallite shape was refined using the Popa[48] line broadening model. A 183(5) Å-edge cubic mean shape was obtained, which corresponds to a mean coherent size of 296(8) Å along [111] and a tenth of the nominal thickness of the layer. We obtained correlatively a slightly larger isotropic mean micro strain level [1.9(1) 10^{-4} rms] compared to the BST layer on sapphire substrate. Both smaller crystallite sizes and larger micro strains are signatures of a poorer crystalline state for the BST film exhibiting a fiber texture. The $\sigma^{M}{}_{11}$ and $\sigma^{M}{}_{22}$ macroscopic residual stresses of the BST layer are refined at 346(8) and 348(8) MPa, respectively and can be considered equivalent, along the main Si [100] directions in the film plane. This layer is then placed under biaxial extension on the Pt layer, this latter exhibiting $\sigma^{M}{}_{11} = 867(2)$ MPa and $\sigma^{M}{}_{22} = 882(2)$ MPa being itself at strong extensions. The BST residual stress regime is then strongly influenced by the substrate-imposed interactions, these latter simultaneously modifying only slightly the texture components.

In film of type 2 the stabilized fiber texture components are very strong in both BST and Pt layers [Figs. 13(a) and 13(b) respectively], but two components exist in each layer. In BST, the ⟨100⟩ fiber orientation dominates, but a ⟨111⟩ component still exists as probably a reminiscence of the substrate influence. The overall texture strength in this layer is much larger than in the other film (film of type 1), pointing to smaller orientation dispersions, but with much lower crystallite sizes. The Pt layer also shows the same tendency, with a major ⟨111⟩ orientation component and a minor ⟨200⟩ fiber component, both strongly oriented. The fiber axes of the textures of both layers in this film of type 2 are slightly inclined with respect to the film's normal, and follow each other. This film appears strongly stressed in tension, but contrarily to film of type 1, in film of type 2 the BST layer is under larger tensile stress than the Pt electrode. The nearly three times more stressed state of the BST layer (compared to film of type1) is also achieved within cubic crystal symmetry. Table VI resumes the main properties obtained by combined analysis. The residual stresses in the epitaxial BST film is very important, this is currently observed with epitaxial film, the mean crystallites size are very fine for BST films of type 2. Since the tunability is very sensitive to the film stresses; the tunability of BST (111), (100) or epitaxial films must be completely different.

To illustrate the dependence between the structure and the electrical performances, we compare the film electrical properties and in particular the tunability of two structures: BST deposited on sapphire with or without TiO_x buffer layer. We have recently developed a rigorous method to extract the intrinsic properties (dielectric permittivity, losses, tunability and factor of merit) of BST thin films at micro waves frequencies[49,50] up to 60 GHz. Our approach is based on the fabrication on BST films of co-planar waveguide (CPW) transmission lines. A two dimensional tangential vector finite

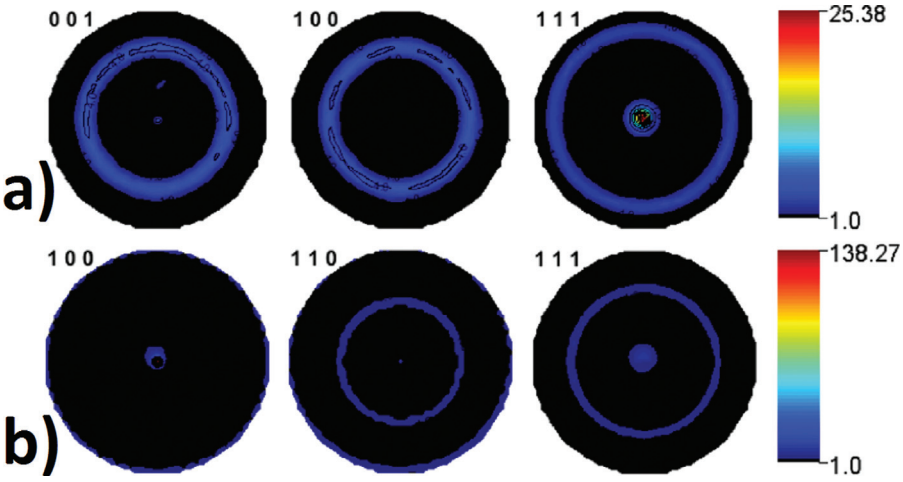

FIG. 12. (Color online) Main axes pole figures for BST (a) and Pt (b) layers of type 1 sample. Linear density scale, equal-area projection.

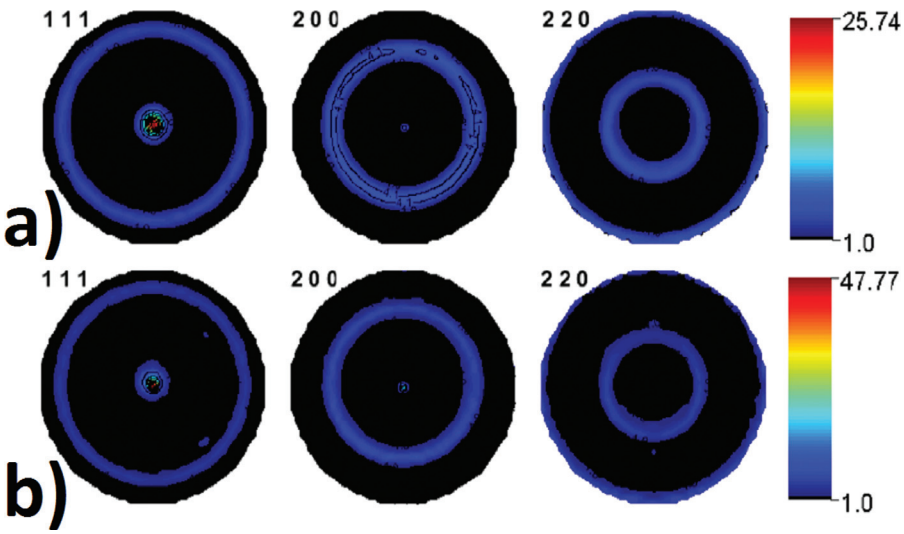

FIG. 13. (Color online) Main axes pole figures for BST (a) which correspond to sample of type 2 — (001) preferred oriented and Pt (b) layers. Linear density scale, equal-area projection.

element method coupled with the homemade specific software Elfi permit to determine the main electrical properties of the films. The results are independent of the top and bottom electrodes and the interfaces. However, our new experimental design can only be applied to BST films directly deposited on (001)-alpha-Al_2O_3 with or without TiO_x, i.e., without the presence of a bottom electrode. Consequently, the electrical results presented here concern films which present a pronounced (111) epitaxial-texture (Fig. 10) or a multicomponents texture (as seen from Fig. 8). Figures 14, 15, and 16 are relative to the dielectric permittivity, losses, and tunability respectively at 1, 5, 15, and 30 GHz. From these results it is clear that the electrical properties are very sensitive to the film structure. The relative dielectric permittivity is larger on BST deposited on sapphire with TiO_x buffer layer: 550 in comparison to 320 when BST is deposited directly on (001)-alpha-Al2O3. This increase is accompanied by a smaller half-width of the curve versus imposed electric field when using the buffer layer, associated to the stronger texture and in-plane alignment giving rise to larger crystallinity for the BST film deposited on TiO_x/Al_2O_3. This larger crystallinity consequently results in larger ϵ values in the whole applied field range. For this film, the relative decrease of ε with frequency is a bit more pronounced (18%) than in the film deposited directly on (001)-alpha-Al_2O_3 (15%). However, even at 30 GHz, using the TiO_x buffer allows a permittivity about 1.6 times larger than without. The loss factor seems larger with presence of the buffer layer but the difference remains very weak, and this tendency seems to reverse at the lowest frequencies. The large tan δ values observed in this microwave frequency range could be due to both intrinsic (due to the interaction of the ac field phonons, including quasi-Debye losses) and/or extrinsic (e.g., mobile charged defects, such as oxygen vacancies) phenomena.[51] The tunability reaches (circled values on the figure) 45% at 30 GHz and 250 kV/cm for the (111) epitaxially textured BST film in comparison to 30% for the other film, and the frequency dependence is relatively attenuated when using TiO_x. The tunability performance of the (111) epitaxially textured film is larger than polycrystalline film. This result is in agreement with the relation between film orientation and tunability performance: the BST films with

TABLE VI. Main parameters of the different BST films extracted from the fine x-ray analysis.

Sample	OD min (m.r.d.)	OD max (m.r.d.)	F^2 (m.r.d.^{2})	Cell parameters (Å)	Residual stresses (MPa)	Mean crystallite size (Å)
BST on sapphire	0	306	2040	4.00817(3)	$\sigma^M{}_{11} = -2330(20)$ $\sigma^M{}_{22} = -2400(20)$	463.7(9)
BST/Pt/Si type 1						
BST	0	160	12	$a = 3.96447(5)$ $c = 3.99892(7)$	$\sigma^M{}_{11} = 346(8)$ $\sigma^M{}_{22} = 348(8)$	183(5) [100] 296(8) [111]
Pt	0	103	17	$a = 3.90023(1)$	$\sigma^M{}_{11} = 867(2)$ $\sigma^M{}_{22} = 882(2)$	1200
BST/Pt/Si type 2						
BST	0	426	53.3	3.9874(3)	$\sigma^M{}_{11} = 970(77)$ $\sigma^M{}_{22} = 888(74)$	82(3) [100] 120(5) [111]
Pt	0	705	42.5	3.90635(1)	$\sigma^M{}_{11} = 217(2)$ $\sigma^M{}_{22} = 265(3)$	858(5)

Parentheses indicate r.m.s. standard deviation on the last digit.

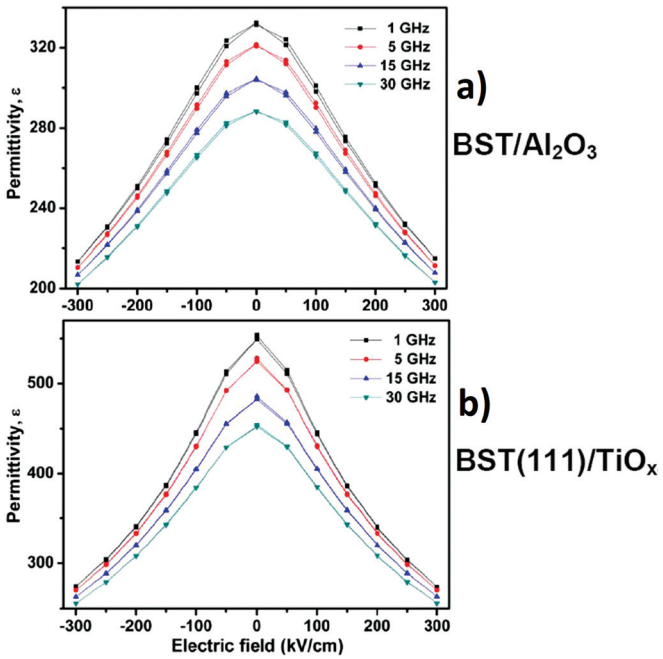

FIG. 14. (Color online) Variation of the permittivity as a function of the applied electric field for BST films deposited on (001)-alpha-Al_2O_3 substrates with or without TiO_x buffer layer (5 nm thick) at 1, 5, 15, and 30 GHz.

(111) preferred orientation present larger tunability rather than polycrystalline BST films. It is more difficult to compare the tunability between (111) preferred oriented film and (111) epitaxially textured film; the stresses must play an important role. Maybe other parameters such as the micro structure (grain size) can also influence the electrical performances. But for the moment we cannot provide more electrical information on the films deposited on Pt-electrodes

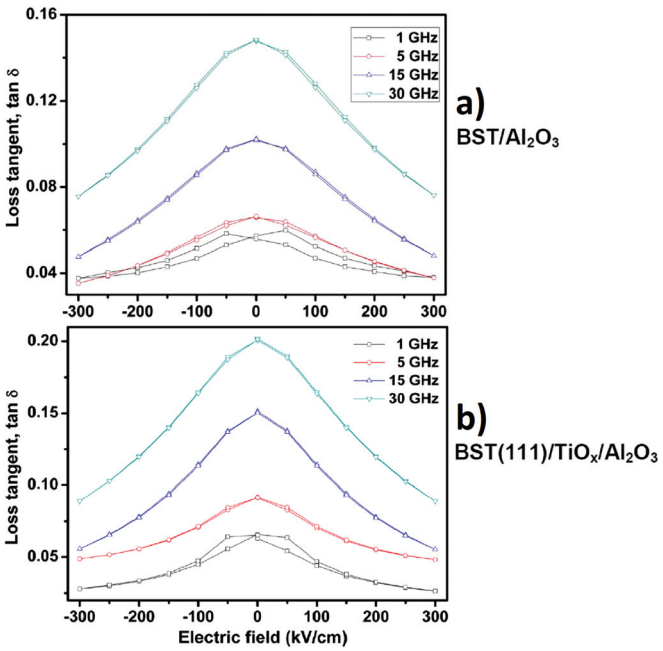

FIG. 15. (Color online) Variation of the loss tangent as a function of the applied electric field for BST deposited on (001)-alpha-Al_2O_3 substrate with or without TiO_x buffer layer (5 nm thick) at 1, 5, 15, and 30 GHz.

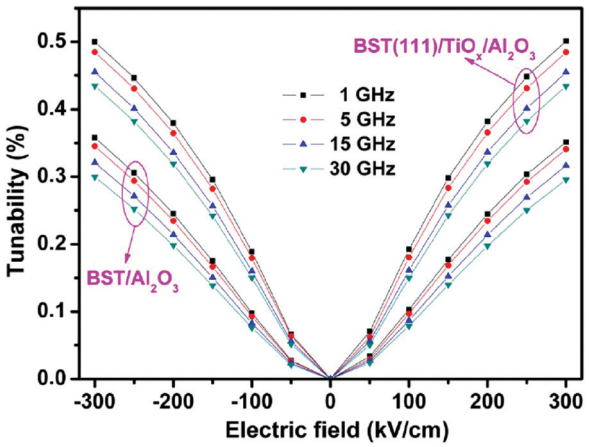

FIG. 16. (Color online) Variation of the tunability as a function of the applied electric field for BST films deposited on (001)-alpha-Al_2O_3 substrates with or without TiO_x buffer layer (5 nm thick) at 1, 5, 15, and 30 GHz.

since we must design a new architecture of the circuit in this case (micro ridge wave guide). This work is now in progress.

The results presented in this paper show clearly the structural and the micro structural properties differences between BST films preferentially oriented with the (111) or (100) planes parallel to the sample in a fiber-texture component, and (111) epitaxial films. The comparison of the electrical properties of a multi components- film and a (111) epitaxially textured films show important differences in film performances, in terms of dielectric permittivity, losses, and tunability. It is very difficult for the moment to know precisely which parameters induce the main important effect: stresses, grain size, etc.

IV. CONCLUSION

We have demonstrated in this work the possibility to monitor the BST film orientation from (001) to (111) on Si/SiO_2/TiO_x/Pt substrates using introduction of O_2 in the plasma or using a TiO_x buffer layer. On (001)-alpha-Al_2O3 substrate covered with a very thin TiO_x buffer layer the BST films present an epitaxial-like character. X-ray combined analysis of the BST films which present ⟨111⟩ fiber texture or an epitaxial (111) texture show important differences as well in terms of orientation distribution of the crystallites as of the presence of residual stresses. As a consequence the elastic coefficients are completely different for (001), (111), or epitaxial BST films. The electrical measurements show that the tunability is very sensitive to the film orientation and the stresses in the ferroelectric films. Since in our study many parameters influence the tunability performances, it is not easy to conclude what parameters (stresses, grain size, etc.) have the major effect. The epitaxial nature of the film seems improve the relative permittivity, the tunability but the losses are degraded; we cannot compare with BST monocrystal since in thin film form the stresses play an important role. We demonstrate clearly that the *in situ* rf sputtering process is very well adapted to produce BST films witch present finely monitored micro structural properties. More studies are now in progress to correlate more largely [extended to

(111) or (001)-preferred orientation and (111) or (100) epitaxially textured] the structural and the electrical properties of BST films with the design of new circuit architecture (microstrip lines).

ACKNOWLEDGMENTS

The authors want to thank The National Natural Science Foundation of China (No. 10974215) and Advance Research Project of Chinese Academy of Sciences (No. CXJJ-11-Q87), the French Education Ministry for the PhD student financial support, and The Conseil Régional de Basse Normandie for partial financial support of the 4-circles Combined Analysis diffractometer.

[1]A. K. Tagantsev, V. O. Sherman, K. F. Astafiev, J. Venkatesh, and N. Setter, J. Electroceram. **11**, 5 (2003).
[2]M. J. Lancaster, J. Powell, and A. Porch, Supercond. Sci. Technol. **11**, 1323 (1998).
[3]C. L. Canedy, H. Li, S. P. Alpay, L. Salamanca-Riba, A. L. Roytburd, and R. Ramesh, Appl. Phys. Lett. **77**, 1695 (2000).
[4]D. R. Patil, S. A. Lokare, R. S. Devan, S. S. Chougule, C. M. Kanamadi, Y. D. Kolekar, and B. K. Chougule, Mater. Chem. Phys. **104**, 254 (2007).
[5]H.-S. Kim, H.-G. Kim, I.-D. Kim, K.-B. Kim, and J.-C. Lee, Appl. Phys. Lett. **87**, 212903 (2005).
[6]H.-S. Kim, H.-G. Kim, I.-D. Kim, K.-B. Kim, and J.-C. Lee, Appl. Phys. Lett. **87**, 212903 (2005).
[7]C. L. Chen, H. H. Feng, Z. Zhang, A. Brazdeikis, Z. J. Huang, W. K. Chu, C. W. Chu, F. A. Miranda, F. W. Van Keuls, R. R. Romanofsky, and Y. Liou, Appl. Phys. Lett. **75**, 412 (1999).
[8]M. W. Cole, W. D. Nothwang, C. Hubbard, E. Ngo, and M. Ervin, J. Appl. Phys. **93**, 9218 (2003).
[9]Y. Wang, B. T. Liu, F. Wei, Z. M. Yang, and J. Du, Appl. Phys. Lett. **90**, 042905 (2007).
[10]W. Choi, B. S. Kang, Q. X. Jia, V. Matias, and A. T. Findikoglub, Appl. Phys. Lett. **88**, 062907 (2006).
[11]C. L. Chen, J. Shen, S. Y. Chen, Z. Zhang, G. P. Luo, W. K. Chu, and C. W. Chu, Ferroelectrics **252**, 181 (2001).
[12]C. L. Chen, J. Shen, S. Y. Chen, G. P. Luo, C. W. Chu, F. A. Miranda, F. W. Van Keuls, J. C. Jiang, E. I. Meletis, and H. Y. Chang, Appl. Phys. Lett. **78**, 652 (2000).
[13]M. Morales, D. Chateigner, and L. Lutterotti, Mater. Sci. Forum **113**, 408–412 (2002).
[14]D. Chateigner, *Combined Analysis* (ISTE-Wiley, London, 2010), p. 497.
[15]L. Lutterotti, S. Matthies, and H.-R. Wenk, *MAUD (Material Analysis Using Diffraction): A User Friendly Java Program for Rietveld Texture Analysis and More*, edited by J. A. Spunar (National Research Council of Canada, Ottawa, 1999), p. 1599.
[16]W. D. Fei, C. Q. Liu, M. H. Ding, W. L. Li, and L. D. Wang, Rev. Sci. Instrum. **80**, 093903 (2009).
[17]M. Field and M. E. Merchant, J. Appl. Phys. **20**, 741(1949).
[18]J.-H. Bae, S. H. Choi, and K.B. Kang, Mater. Sci. Forum 215, **408-412**, 1179 (2002).
[19]M. Birkholz, J. Appl. Cryst. **40**, 735 (2007).
[20]M. Birkholz, *Thin Film Analysis by X-ray Scattering* (Wiley-VCH, New York, 2006), p. 356.
[21]A. Le Bail, Powder Diffr. **20**, 316 (2005).
[22]S. Matthies, G. Vinel, and K. Helming, *Standard Distributions in Texture Analysis*, edited by Matthies, Vinel, Helming (Akademie-Verlag, 1987), Vol. 1, p. 449.
[23]R. Hielscher, H. Schaeben, and D. Chateigner, J. Appl. Cryst. **40**, 371 (2007).
[24]L. Lutterotti, D. Chateigner, S. Ferrari, and J. Ricote, Thin Solid Films **450**, 34 (2004).
[25]H. Schaeben, "Determination of complete ODF using the maximum entropy method," in *Advances and Applications of Quantitative Texture Analysis*, edited by H.-J. Bunge and C. Esling (DGM, Oberursel, Germany, 1991), pp. 109–118.
[26]L. Lutterotti, Nucl. Instrum. Methods Phys. Res. B **268**, 334 (2010).
[27]E. Guilmeau, D. Chateigner, T. S. Suzuki, Y. Sakka, C. Henrist, and B. Ouladdiaf, Chem. Mater. **17**, 102 (2005).
[28]D. Chateigner, J. Appl. Crystallogr. **38**, 603 (2005).
[29]S. Grazulis, D. Chateigner, R. T. Downs, A. F. T. Yokochi, M. Quiros, L. Lutterotti, E. Manakova, J. Butkus, P. Moeck, and A. Le Bail, J. Appl. Crystallogr. **42**, 726 (2009).
[30]S. Matthies and M. Humbert. J. Appl. Crystallogr. **28**, 254 (1995).
[31]U. F. Kocks, C. N. Tomé, and H.-R. Wenk, *Texture and Anisotropy* (Cambridge University Press, Cambridge, 1998), p. 676.
[32]U. Welzel, J. Ligot, P. Lamparter, A. C. Vermeulen, and E. J. Mittemeijer, J. Appl. Cryst. **38**, 1 (2005).
[33]R. Yokoyama, J. Harada, and Y. Akiniwa, Powder Diffr. **25**, 25 (2010).
[34]K. J. Martinschitz, R. Daniel, C. Mittererb, and J. Keckes, J. Appl. Cryst. **42**, 416 (2009).
[35]C. Q. Liu, W. L. Li, and W. D. Fei, Acta Mater. **58**, 5393 (2010).
[36]Z.-G. Ban and S. P. Alpay, J. Appl. Phys. **91**, 9288 (2002).
[37]T. Çağın, Phys. Rev. B **59**, 3468 (1999).
[38]A. L. Campbell, R. R. Biggers, G. Subramanyam, G. Kozlowski, R. A. Kleismit, H. N. Zate, S. C. Hopkins, B. A. Glowacki, B. D. Riehl, and T. L. Peterson, Nanotechnology **19**, 485704 (2008).
[39]J. Hiltunen, D. Seneviratne, H. L. Tuller, J. Lappalainen, and V. Lantto, J. Electroceram. **22**, 395 (2009).
[40]K. B. Kim, T. S. Yun, J. C. Lee, H. S. Kim, H. G. Kim, and I. D. Kim, IEEE Trans. Ultrason. Ferrolectr. Freq. Control **53**, 518 (2006).
[41]H. S. Kim, H. G. Kim, K. B. Kim, and J. C. Lee, Appl. Phys. Lett. **87**, 212903 (2005).
[42]I. D. Kim, H. L. Tuller, H. S. Kim, and J. S. Park, Appl. Phys. Lett. **85**, 4705 (2004).
[43]L. Yang, G. Wang, D. Rémiens, and X. Dong, J. Am. Ceram. Soc, **93**, 350 (2010).
[44]L. Yang, G. Wang, D. Rémiens, and X. Dong, J. Am. Ceram. Soc., **93**, 350–352 (2010).
[45]J. Li, J. Yu, G. Peng, Y. B. Wang, and W. L. Zhou, J. Am. Ceram. Soc. **90**, 3220 (2007).
[46]M. Morales, P. Laffez, D. Chateigner, and I. Vickridge, Thin Solid Films **418**, 119 (2002).
[47]V. Bornand, I. Huet, J.-F. Bardeau, D. Chateigner, and Ph. Papet, Integr. Ferroelectr. **43**, 51 (2002).
[48]N.C. Popa, J. Appl. Crystallogr. **31**, 176 (1998).
[49]F. Ponchel, J. Midy, J. F. Legier, C. Soyer, D. Rémiens, T. Lasri, and G. Guéguan, J. Appl. Phys. **107**, 054112 (2010).
[50]F. Ponchel, J.-F. Legier, C. Soyer, D. Rémiens, J. Midy, T. Lasri, and G. Guéguan, Appl. Phys. Lett. **96**, 1 (2010).
[51]A. K. Tagantsev, V. O. Sherman, K. F. Astafiev, J. Venkatesh, and N. Setter, J. Electroceram. **11**, 5 (2004).